applied sciences

MDPI

Article

Influence of Surface Roughness on Surface Energy and Work Function of Tungsten Based on First-Principles Study

Andrey A. Kistanov *, Rinat Kh. Khisamov and Radik R. Mulyukov

Institute for Metals Superplasticity Problems of Russian Academy of Sciences, 39 Stepan Khalturin st., Ufa 450001, Russia

* Correspondence: andrei.kistanov.ufa@gmail.com

Abstract

The formation of surface morphology under ion irradiation has been widely studied in various metals and metal surfaces. Nanoscale roughening or smoothing of the surface leads to changes in the thermal, electronic, and even antibacterial properties of metallic materials. In this study, first-principles calculations were used to gain insight into the modification of surface dipole moment due to changes in surface roughness for the case of tungsten (W). The physical nature of the change in work function (WF) due to surface roughness was found. For the W(100) surface, it was shown that the negative dipole layer formed on the surface prevents the outflow of electrons from the base metal, which leads to an increase in the WF from 3.92 eV to 4.17 eV with increasing surface roughness. The opposite was observed on the W(110) surface, where the decrease in the WF from 4.76 eV to 4.58 eV is due to a small dipole layer blocking electrons on the surface due to charge redistribution within the base metal. This study evaluates the changes in the electronic properties of W due to its surface modification under the ion beam irradiation, which can be applied in future experiments.

Keywords: surface modification; density functional theory; electron transfer; dipole layer; surface morphology

1. Introduction

Ion-induced surface morphology under ion irradiation is driven by material structure, atomic redistribution and defect creation [1–6]. Driven by the momentum transfer of incident ions, these processes cause nanoscale roughening or smoothing depending on the ion energy, fluence, angle of incidence, and target temperature [7]. In turn, the surface morphology change may lead to a significant modification of thermal, electronic and even antibacterial properties of the material. Ion-induced surface morphology formation has been widely studied in various metals and metal surfaces. It has been shown that the irradiation of nickel [8,9], copper [10], tungsten (W) [11], and titanium [12] with an ultrafine-grained structure with argon ions makes it possible to form a uniform cone-shaped relief of the metal surface. The obtained surface-modified metal structure has shown high thermal stability [13]. For example, cone-shaped relief on the nickel is thermally stable up to 800 °C, reaching a thermal stability threshold of 300 °C, higher than that of the bulk nanostructured nickel [14]. For magnesium and titanium alloys, it has been found that ion irradiation of the surface morphology results in deep subsurface hardening which improves the wear resistance of these alloys [15]. It is widely reported that the incorporation of high-aspect-ratio nanostructures into a surface imparts antibacterial properties to it. For example, it

Academic Editors: Luca Spiridigliozzi and Sebastiano Candamano

Received: 22 June 2026
Revised: 19 July 2026
Accepted: 23 July 2026
Published: 27 July 2026

has been found that nanospikes with a height of about 300 nm, an apex radius of about 60 nm, a base radius of about 90–140 nm, and an interspike distance of 200 to 400 nm effectively destroy attached bacteria [16]. The study [17] has demonstrated a new approach to obtaining an antibacterial nano-spike surface by titanium bulk nanostructuring followed by ion irradiation. It has been found that 200 nm high nanospikes, uniformly distributed at a distance of 100 nm, damage the bacterial cell wall and penetrate *E. coli*, resulting in micro-sized *E. coli* bacteria which are unable to survive on such a uniform surface.

Ion irradiation-induced pattern formation on cobalt surfaces was discussed in [18]. The formation of cone-shaped structures developing with increasing fluence in aluminum irradiated with a helium ion beam was shown in [19]. Several studies examined W, which, due to its high melting point, thermal conductivity, and relatively low sputtering and thermal expansion coefficients, is a promising material for plasma-processing parts of fusion reactors [20]. In [21], it was demonstrated that castle-like structures with strong asymmetry and with the height of >200 μm can be formed in W exposed to an intense argon ion beam with average energy of 2 keV and etched through in the center. Recently, the main mechanisms determining the evolution of defects and the deterioration of the mechanical properties of W in operating conditions under the helium ion irradiation have been revealed [22]. However, there is still a need in assessing the influence of ion irradiation-induced surface roughness on the work function (WF) of W at the atomic level.

The electron WF, associated with the Fermi level, is a vital parameter in surface physics and solid-state chemistry and is one of the most fundamental electronic properties of a material. The influence of surface roughness on the WF of aluminum–magnium alloys was investigated in [23] using the Kelvin scanning probe method and theoretical modeling. Using the least squares method, it was shown that the WF increases linearly with the increase in surface roughness. At the atomic level, calculations based on density functional theory demonstrated a correlation between increasing surface roughness and decreasing gold WF [24]. The observed decrease in the WF compared to its initial value indicates the transition of noble gold into a chemically active metal, which is due to a change in the distribution of energy bands, facilitating the release of electrons from the surface.

The WF of materials is widely used to characterize various phenomena such as adhesion, corrosion, wear, and interfacial bonding due to its high sensitivity to surface morphology [25]. From a physical point of view, the WF of a surface is profoundly associated with the surface dipole, an electrostatic potential barrier created by charge redistribution and leakage of electrons into vacuum. The sensitivity of the surface dipole depends on the outermost layers of the surface exposed to the environment, such as surface defects and surface oxidation [26–28]. On the other hand, the WF of a material is strongly dependent on the surface roughness, while the basic WF is determined by the type of material and its crystal faces; surface roughness causes microscopic physical changes that significantly alter electron emission [29]. Despite numerous theoretical studies aimed at investigating the correlation between WF and surface morphology [30], the understanding of the influence of surface roughness on the WF of W remains insufficient. In particular, the influence of surface roughness on the WF can be assessed by a comprehensive comparison of WF calculations with quantitative and qualitative charge analysis [24].

In this study, the relationship between surface roughness and WF of W has been evaluated using first-principles calculations. In addition, the underlying reasons for the change in the WF depending on the surface roughness have been revealed at the atomic level, and the role of the surface dipole in this mechanism has been assessed. The combination of WF calculations with Bader charge analysis and ELF provides a mechanistic explanation for the WF trends observed for the W(100) and W(110) surfaces.

2. Materials and Methods

The first-principles calculations were performed in the framework of density functional theory using the open-source Quantum Espresso computer code [31,32]. The ultrasoft [33] pseudopotential W_pbe_v1.2.uspp.F.UPF from the GBRV-1.2 library [34] of the standard solid state PPs precision collection [35] was used. The first Brillouin zone was sampled with a 2×2×2 k-mesh grid. Periodic boundary conditions were used to approximate an infinitely large system. The vacuum space of 15 Å was set in the direction perpendicular to the surface plane to avoid periodic image interactions, artificial electrostatic overlap, spurious mirror-image bonding, and inaccurate electronic properties. The bottom three layers of the considered cone-shaped structures were fixed to describe bulk effects. The kinetic energy cut-off was set to 520 eV. A Gaussian broadening width of occupation of the electron level of 0.2 eV was set. The chosen computational parameters are largely standardized and widely accepted in DFT modeling of tungsten [36]. All the considered structures were fully optimized until forces acting on each atom were smaller than 10^{-6} a.u., the change in the total energy was less than 10^{-8} a.u. and the absolute value of the pressure was less than 10^{-5} a.u.. Specific convergence criteria were established based on the Quantum ESPRESSO user manual and were well below standard limits, ensuring high ground state accuracy. The model sizes were set so that the reliable nano-hillocks structures were created but the computational cost of the calculations was still affordable. Specifically, 4×4 and 5×7 supercells were used in the case of the W(100) and W(110) surfaces, respectively. In these supercells, W atoms were removed to form a nano-hillock structure. The outer/inner angles of a nano-hillock structure were determined based on the available cell size. It should be noted, a limitation of our model is that, due to the high cost of calculations, the structure built is not large enough to simulate, for example, cone-shape surfaces similar to those observed experimentally [8–12]. Since W is a diamagnetic material, an initial magnetic moment of 0 μB is assigned for each W atom. Bader charge analysis was utilized to estimate the electron charge within each atomic volume. Structural and volumetric data were treated and visualized using the VESTA 3 program. The lattice constant of the body-centered cubic W calculated in this work is 3.165 Å, which is close to the values (3.160 Å–3.180 Å) reported in theoretical and experimental studies [37–40].

3. Results

Figure 1 shows the W surfaces considered in this work with different surface morphology and roughness. Figure 1a,d show pure W(100) and W(110) surfaces. Figure 1b,e show the W(100) and W(110) surfaces with the outer angle/inner angles are 73°/54° (R1 structure) and 93°/44° (R2 structure), respectively (Table 1). Figure 1c,f show the W(100) and W(110) surfaces with the outer angle/inner angles are 82°/49° (R2 structure) and 91°/45° (R4 structure), respectively (Table 1).

Table 1. Surface morphology, surface energy and WF of the considered surfaces.

Surface	Slope (Outer Angle/Inner Angle)	Surface Energy, eV/A^2	WF, eV
Pure W(100)	-	0.202	3.92
R1 W(100)	73°/54°	0.153	4.06
R2 W(100)	82°/49°	0.124	4.17
Pure W(110)	-	0.197	4.76
R3 W(110)	93°/44°	0.320	4.61
R4 W(110)	91°/45°	0.343	4.58

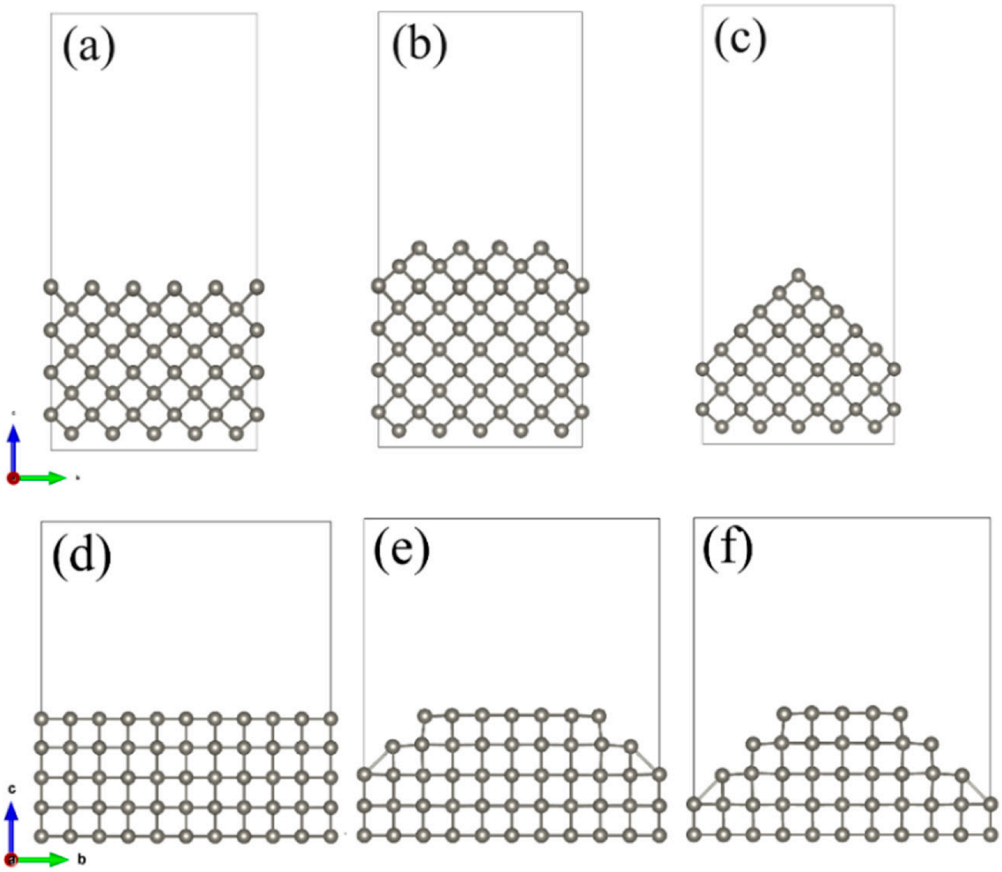

Figure 1. Side and top views of atomic structures of a pure (**a**), R1 (**b**), and R2 (**c**) W(100) surfaces. Side and top views of atomic structures of a pure (**d**), R3 (**e**), and R4 (**f**) W(110) surfaces.

First, the surface energy, which is defined as the energy associated with the interaction of ions with a surface, influenced by the surface potential and the intrinsic chemical affinity of reactive sites at the surface [41], is calculated for each considered surface as follows [42]:

$$E_{surf} = \frac{\left[E_{slab} - \left(\frac{N_{slab}}{N_{bulk}}\right).E_{bulk}\right]}{2A} \quad (1)$$

where E_{slab} and E_{bulk} represent the total energies of the surface slab and the bulk unit cell, respectively; N_{slab} and N_{bulk} are the numbers of atoms contained in the slab and the bulk unit cells, respectively; A is the unit area of the surface.

Table 1 collects the surface energy value of all the structures considered. Among pure W surfaces, the W(100) surface possesses the highest surface energy of 0.202 eV/A^2, and the lowest surface energy of 0.197 eV/A^2 is found for the W(110) surface. The obtained results largely coincide with the results of previous theoretical studies, verifying our theoretical model [43]. Next, changes in surface energy depending on surface morphology are considered. The R1 W(100) surface has a lower surface energy of 0.153 eV/A^2 (Table 1) compared to the case of a pure W(100) surface. The surface energy of the R2 W(100) surface further decreases to 0.124 eV/A^2 (Table 1) with the increase in the surface roughness. This may be due to passivated bonds along the surface contour [44,45]. Conversely, the surface energy of the R3 W(110) and R4 W(110) surfaces increases to 0.320 eV/A^2 and 0.343 eV/A^2 (Table 1) compared to the case of a pure W(110) surface. This can be attributed to the presence of dangling bonds along the surface contour [46]. Surface roughness affects the WF of metals, including W, by changing the effective surface area and influencing factors such as electron emission [47,48]. According to Table 1, the pure W(100) surface has a WF

value of 3.92 eV, which is consistent with previous studies, where it varies from 3.98 eV to 4.11 eV [49,50]. The WF value for the W(110) surface is found to be 4.76 eV, which is consistent with previous studies, where it is found to be 4.81 eV [50]. Note, the WF value for the W(110) surface is higher than that for the W(100) surface. A less stable, more reactive surface, such as a W(100) surface, has a lower WF, while a more stable and less reactive surface, such as a W(110) surface, has a higher WF. Therefore, a more stable surface has lower surface energy and higher productivity.

With the increase in surface roughness, the WF of the W(100) surface increases to 4.06 eV in the case of the R1 structure and to 4.17 eV in the case of the R2 structure (Figure 2a). In the case of the W(110) surface, an increase in surface roughness leads to a decrease in the WF to 4.61 eV in the case of the R3 structure and to 4.58 eV in the case of the R4 structure (Figure 2b). Therefore, for the W(100) surface, the WF increases linearly with the increase in surface roughness, while for the W(110) surface, the WF decreases linearly with the increase in surface roughness. This difference can be attributed to the distinct atomic arrangements and electron densities at the surface of these crystallographic planes [51–54].

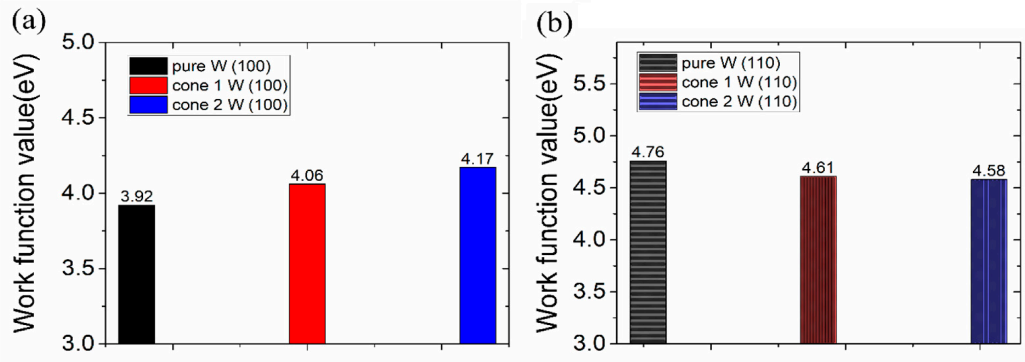

Figure 2. Diagrams with the WF values for a pure, R1, and R2 W(100) surfaces (**a**) and for a pure, R1, and R2 W(110) surfaces (**b**).

To deeper understand the change in the WF associated with the surface roughness affecting electron densities at the surface of the considered crystallographic planes, electron localization function (ELF) and Bader charges of the considered surfaces are analyzed. The 2D plot of the ELF of the pure W(100) surface is shown in Figure 3a–c. It reflects the electron localization on the atoms of the uppermost layer and the decrease in the electron localization with an increase in the number of the layer from the surface to center of the bulk. In ELF plots, dangling bonds appear as localized, asymmetrical "lobes" projecting outward from atoms of the surface. Dangling bonds localized on surface atoms dictate the surface dipole moment, which directly shifts the local vacuum level and alters the WF. According to Figure 3a, surface atoms have ELF maxima (red "lobes") extending into the vacuum, which confirms the presence of dangling bonds. The Bader charge analysis also indicates electron accumulation of ~0.23 *e* per atom by the atoms of the uppermost layer and of ~0.21 *e* per atom by the atoms of the second layer. On the other hand, the atoms of the third, fours, and fifth layers lose ~0.12 *e* per atom, ~0.07 *e* per atom, and ~0.04 *e* per atom, respectively. Therefore, in the case of the pure W(100) surface, a charge transfer from the inner layers to the uppermost layer is found.

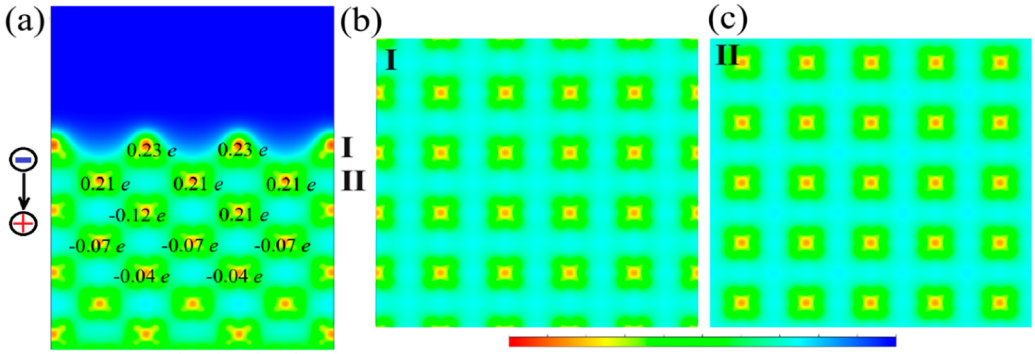

Figure 3. The 2D plots of the ELF of the pure W(100) surface. Side view of the structure (**a**) and top views for layers I (**b**) and II (**c**). The color bar indicates the level of ELF. A positive charge value indicates a gain of electrons, while a negative charge value indicates a loss of electrons.

Figure 4a–d depict the 2D plots of the ELF of the R1 W(100) surface. The atoms in the uppermost layer gain electrons from the atoms of the inner layers. On the surface, isolated ELF maxima (top most atoms in Figure 4a,) stretching into the vacuum are visible, which confirms the presence of dangling bonds. The Bader charge analysis indicates an accumulation of ~0.14 *e* per atom by the atoms in the middle of the uppermost layer and of ~0.32 *e* per atom and ~0.47 *e* per atom by the atoms at the edge of the uppermost layer (Figure 4b). The atoms in the middle of the second layer lose ~0.20 *e* per atom and atoms at the edge of the second layer lose ~0.10 *e* per atom (Figure 4c). The atoms of the third layer almost do not participate in the charge redistribution, losing only about 0.03 *e* per atom (Figure 4d). Therefore, in the case of the R1 W(100) surface, a strong charge transfer from the second layer to the uppermost layer is found.

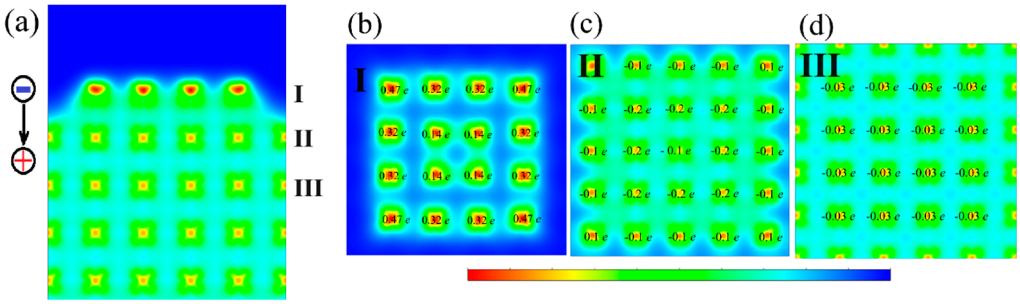

Figure 4. The 2D plots of the ELF of the R1 W(100) surface. Side view of the structure (**a**) and top views for layers I (**b**), II (**c**), and III (**d**). The color bar indicates the level of ELF. A positive charge value indicates a gain of electrons, while a negative charge value indicates a loss of electrons.

Figure 5a–f present the 2D plots of the ELF of the R2 W(100) surface. In that case, more atomic layers are considered due to the presence of atoms with dangling bonds and redistributed charge in these layers as the height of the R2 structure increases compared to the R1 structure. On the surface, isolated ELF maxima (top most atom in Figure 5a) stretching into the vacuum are visible, confirming the presence of dangling bonds. The atoms in the uppermost layer gain electrons from the atoms of the inner layers. The Bader charge analysis indicates an accumulation of ~0.30 *e* per atom by the atoms in the middle of the uppermost layer and of ~0.47 *e* per atom by the atoms at the edge of the uppermost layer (Figure 5b). The atoms in the middle of the second layer lose ~0.12 *e* per atom, while the atoms at the edge of the second layer gain ~0.17 *e* per atom (Figure 5c). The atoms of the third layer, different from the case of the R1 W(100) surface, are involved in the charge redistribution. The atoms in the middle of the third layer lose up to 0.38 *e* per atom, while the atoms at the edge of the third layer gain up to 0.17 *e* per atom (Figure 5d). In the fourth

layer, a charge loss by the middle atoms up to 0.16 *e* per atom is observed, while the edge atoms gain up to 0.14 *e* per atom (Figure 5e). In the fifth layer, a charge loss of 0.10 *e* per atom and 0.15 *e* per atom by the middle atoms is observed, while six edge atoms gain up to 0.13 *e* per atom (Figure 5f). The atoms of the sixth layer almost do not participate in the charge redistribution. Therefore, in the case of the R2 W(100) surface, in addition to a strong charge transfer from the inner layer to the upper layer, a charge transfer from the inner atoms to the edge atoms is found.

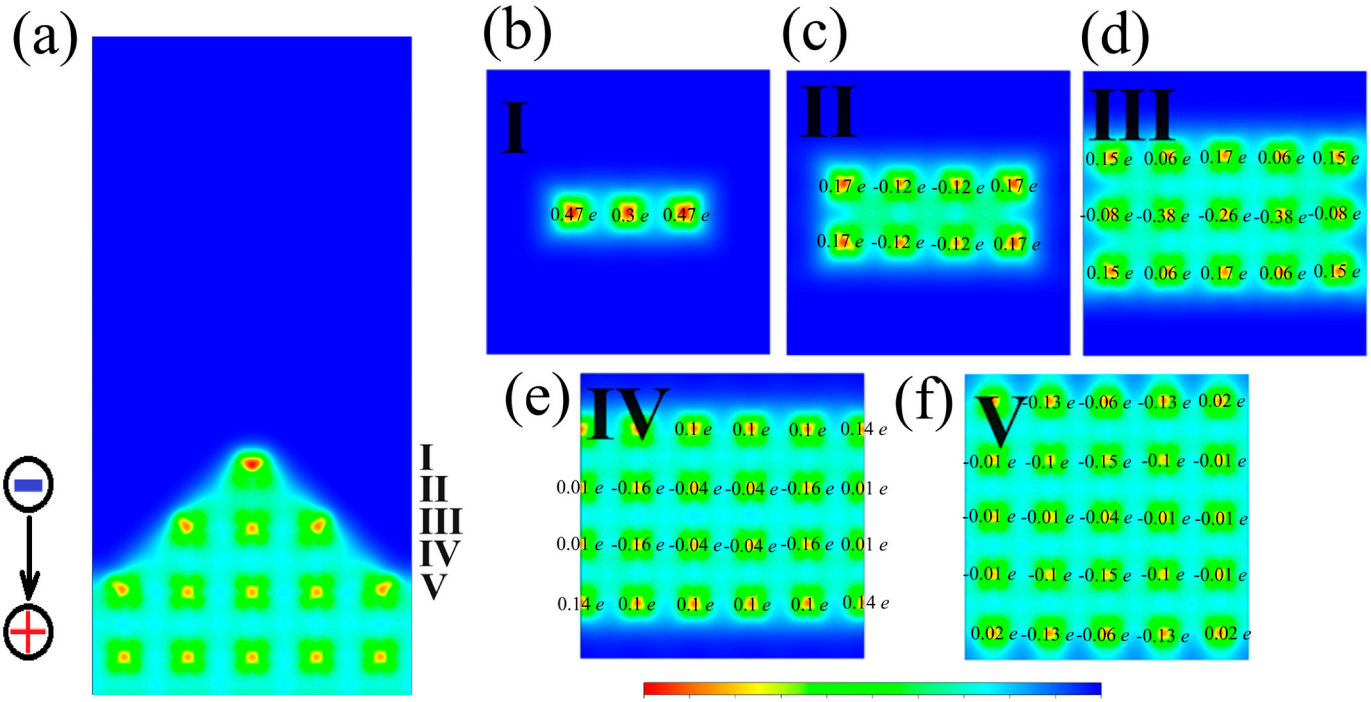

Figure 5. The 2D plots of the ELF of the R2 W(100) surface. Side view of the structure (**a**) and top views for layers I (**b**), II (**c**), III (**d**), IV (**e**), and V (**f**). The color bar indicates the level of ELF. A positive charge value indicates a gain of electrons, while a negative charge value indicates a loss of electrons.

The 2D plots of the ELF of the pure W(110) surface are shown in Figure 6a–c. The electron localization on the atoms of the uppermost layer and the decrease in the electron localization in the second layer are found. The Bader charge analysis also indicates electron accumulation of ~0.10 *e* per atom by the atoms of the uppermost layer and electron loss of ~0.10 *e* per atom by the atoms of the second layer. On the other hand, there is no charge transfer from the atoms of the third and subsequent atomic layers. Therefore, in the case of the pure W(110) surface, there is a dipole layer that blocks electrons in the bulk and leads to a higher WF compared to the pure W(100) surface.

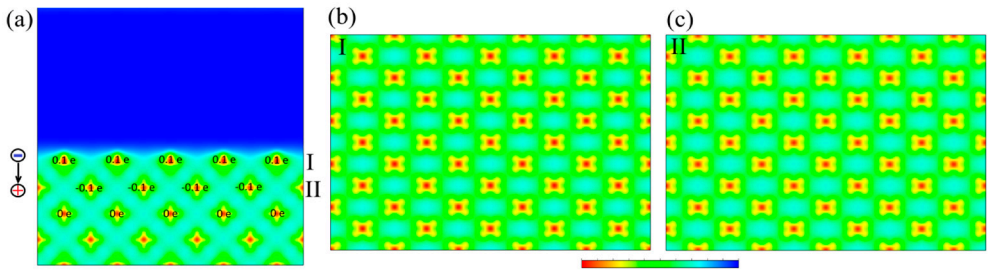

Figure 6. The 2D plots of the ELF of the pure W(110) surface. Side view of the structure (**a**) and top views for layers I (**b**) and II (**c**). The color bar indicates the level of ELF. A positive charge value indicates a gain of electrons, while a negative charge value indicates a loss of electrons.

Figure 7a–d show the 2D plots of the ELF of the R3 W(110) surface. The atoms in the uppermost layer gain electrons from the atoms of the inner layers. Edges on the surface have ELF maxima (red "lobes" in Figure 7a) extending into the vacuum, which confirms the presence of dangling bonds. The Bader charge analysis indicates an accumulation of ~0.10 *e* per atom by the atoms in the middle of the uppermost layer and of ~0.30 *e* per atom by the atoms at the edge of the uppermost layer (Figure 7b). The atoms in the middle of the second layer lose ~0.08 *e* per atom, while the atoms at the edge of the second layer gain ~0.17 *e* per atom (Figure 7c). The atoms in the middle of the third layer almost do not participate in the charge redistribution, with the minor electron loss of ~0.05 *e* per atom, while the atoms at the edge of the third layer lose ~0.12 *e* per atom (Figure 7d). Therefore, in the case of the R3 W(110) surface, not only a strong charge transfer from the second layer to the uppermost layer but also charge transfer from the atoms in the middle of the layers to the edge atoms are found.

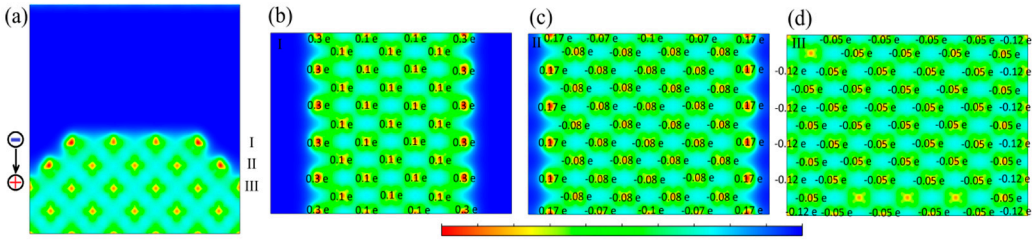

Figure 7. The 2D plots of the ELF of the R3 W(110) surface. Side view of the structure (**a**) and top views for layers I (**b**), II (**c**), and III (**d**). The color bar indicates the level of ELF. A positive charge value indicates a gain of electrons, while a negative charge value indicates a loss of electrons.

The 2D plots of the ELF of the R4 W(110) surface are presented in Figure 8a–e. The atoms in the uppermost layer gain electrons from the atoms of the inner layers. However, there are also two atomic chains in between the edge and central atoms that neither gain nor lose electrons. Edge atoms on the surface have ELF maxima (red "lobes" in Figure 8a) extending into the vacuum, which confirms the presence of dangling bonds. According to the Bader charge analysis, an accumulation of ~0.28 *e* per atom is observed in the edge atoms and ~0.14 *e* per atom in the central atoms of the uppermost layer (Figure 8b). The central atoms in the second layer lose ~0.11 *e* per atom, the atoms of the second layer located between the central and edge atoms lose ~0.17 *e* per atom, while the atoms at the edge of the second layer gain ~0.10 *e* per atom, and the corner edge atoms gain ~0.20 *e* per atom (Figure 8c). The central atoms of the third layer do not participate in the charge redistribution, while the edge atoms gain ~0.17 *e* per atom, and the atoms in two neighboring rows lose ~0.14 *e* per atom and ~0.10 *e* per atom, respectively (Figure 8d). In the fourth layer, a charge loss by the middle atoms is almost negligible, while the edge atoms lose up to 0.19 *e* per atom and the atoms in the neighboring row lose up to 0.10 *e* per atom (Figure 8e). Therefore, in the case of the R4 W(110) surface, in addition to a strong charge transfer from the inner layer to the upper layer, a charge transfer from the inner atoms to the edge atoms of the second and third layers is found. However, different to the case of the R2 W(100) surface, the charge is uniformly distributed at the edge and neighboring atoms.

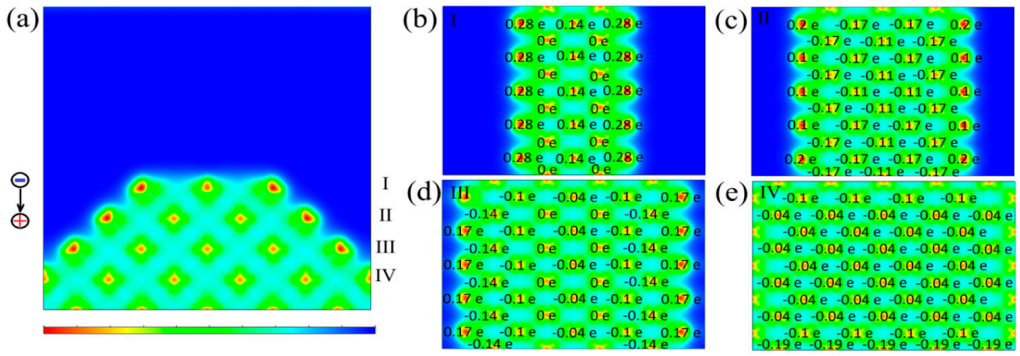

Figure 8. The 2D plots of the ELF of the R4 W(110) surface. Side view of the structure (**a**) and top views for layers I (**b**), II (**c**), III (**d**), and IV (**e**). The color bar indicates the level of ELF. A positive charge value indicates a gain of electrons, while a negative charge value indicates a loss of electrons.

4. Discussion

Under ion beam irradiation, changes to WF are driven by collision cascades, defect accumulation, and surface erosion altering the surface dipole and Wigner–Seitz radius [55]. In particular, when high-energy ions collide with a metal surface, they transfer energy through electronic and nuclear interactions to the outermost atomic layers, changing the surface roughness, nanostructure, and causing simultaneous mixing of atoms. In turn, surface roughness is deeply tied to dangling bonds. Dangling bonds fundamentally break the translational and chemical symmetry of the bulk material, which leads to a shift in the local vacuum level and a change in the WF [28]. Dangling bonds redistribute the electron cloud of the metal, creating localized unsaturated charge and significantly affecting electron emission, catalytic activity and adhesion to the surface [29,56].

Previous theoretical studies have shown that the accumulation of localized electrons at the dangling bond sites alters the surface dipole moment. This effectively lowers the WF of the metal, requiring less energy to release electrons from the surface. For instance, the WF of an iron surface is strongly influenced by coordination number of iron atoms. Surface atoms at the rough surface have dangling bonds and lower coordination numbers, which results in reduced atomic packing density and significantly low the local WF [57]. DFT study has shown correlation between increasing surface roughness and decreasing the WF of gold due to alternation in the distribution of energy bands, facilitating electron escape from the surface [24]. On the other hand, it has been shown that when the WF changes due to roughness induced by variations in geometric characteristics, these changes no longer show a predictable correlation.

This study provides a deeper understanding of the physical mechanism that determines the changes in the WF in W due to changes in surface roughness under ion beam irradiation. In the case of the W(100) surface, the WF increases with the increase in roughness, while in the case of the W(110) surface, it decreases with the increase in roughness. For the case of the W(100) surfaces, when the exterior atoms of a surface gain electrons, this creates an electron accumulation near the surface, forming a negative dipole layer. This negative dipole layer opposes the outflow of electrons from the bulk metal, effectively requiring more energy to remove an electron from the bulk metal, thereby increasing the WF [58]. In the case of the W(110) surface, WF decreases because there is no blocking layer or small dipole blocking electrons on the surface, where charge redistributes between the uppermost layer and the second layer only.

5. Conclusions

In conclusion, the influence of surface roughness resulting from ion irradiation on the surface energy and surface WF was investigated using first-principles modeling. It was found that the WF of the W(100) surface increases with increasing surface roughness, while the WF of the W(110) surface decreases with increasing surface roughness.

The physical nature of the WF change due to surface roughness was also revealed using the Bader and ELF analysis. It was shown that modification of W surfaces, leading to a change in surface roughness, induces a surface dipole moment in the outer layer of the surface, preventing the outflow of electrons from the base metal in the case of the W(100) surface, whereas in the case of the W(110) surface there is a dipole layer blocking electrons on the surface due to charge redistribution within the base metal.

The results of this study contribute to a deeper understanding of the mechanism of metal surface modification under ion beam irradiation and can serve as a useful guide for future experiments.

Author Contributions: Conceptualization, A.A.K. and R.K.K.; methodology, A.A.K.; software, A.A.K.; validation, A.A.K., R.K.K. and R.R.M.; formal analysis, A.A.K. and R.K.K.; investigation, A.A.K.; resources, A.A.K.; data curation, A.A.K.; writing—original draft preparation, A.A.K. and R.K.K.; writing—review and editing, A.A.K., R.K.K. and R.R.M.; visualization, A.A.K.; supervision, A.A.K.; project administration, A.A.K.; funding acquisition, R.R.M. All authors have read and agreed to the published version of the manuscript.

Funding: The present work was accomplished according to the state assignment of IMSP RAS.

Institutional Review Board Statement: Not applicable.

Informed Consent Statement: Not applicable.

Data Availability Statement: The original contributions presented in this study are included in the article. Further inquiries can be directed to the corresponding author.

Conflicts of Interest: The authors declare no conflicts of interest.

References

1. Oluwaleye, O.; Mwakikunga, B.W.; Asante, J.K.O. Effects of Induced Structural Modification on Properties of V+ Ion-Implanted RF—Magnetron Sputtering Deposited ZnO Thin Films of Thickness 120 nm on Borosilicate Glass Substrates. *Nanomaterials* **2025**, *15*, 278. [CrossRef] [PubMed]
2. Bhowmik, D. Morphological Evolution of Silicon Surfaces Nanopatterned by Focused Ion Beam Irradiation. *Sci. Rep.* **2026**, *16*, 4308. [CrossRef] [PubMed]
3. Krasheninnikov, A.V.; Nordlund, K. Ion and Electron Irradiation-Induced Effects in Nanostructured Materials. *J. Appl. Phys.* **2010**, *107*, 71301. [CrossRef]
4. Sedelnikova, M.B.; Kashin, A.D.; Uvarkin, P.V.; Sharkeev, Y.P.; Luginin, N.A.; Khimich, M.A.; Ivanov, K.V. Low-Energy High-Current Electron Beam Treatment of Composite Coatings Based on Diatomite and ZrO_2 Particles. *Lett. Mater.* **2024**, *14*, 216–222. [CrossRef]
5. Liu, Y.; Deng, Y.; Wang, Y.; Wang, L.; Liu, T.; Gong, Z.; Fan, Z.; Wei, H.; Su, Z.; Wei, W.; et al. Surface Self-Assembly of Gold Nanoparticles on Graphite Driven by Ion-Irradiation-Induced Atomic Defects. *Appl. Surf. Sci.* **2025**, *704*, 163442. [CrossRef]
6. Nikolaeva, A.V.; Zykova, A.P.; Shmakov, V.V.; Tarasov, S.Y. Evaluation of Contributions of Hardening Mechanisms to the Yield Strength of Ti6Al4V-Cu Alloys Produced by Wire Electron Beam Additive Manufacturing. *Lett. Mater.* **2024**, *14*, 204–209. [CrossRef]
7. Panchal, V.; Kumar, T.; Sulania, I.; Kumar, S. An Offline Prediction of Nanoscale Ripples Propagation under Ion Irradiation: A Correlation between Ripples Velocity and Surface Erosion Rate. *Vacuum* **2021**, *183*, 109795. [CrossRef]
8. Borisov, A.M.; Mashkova, E.S.; Ovchinnikov, M.A.; Khisamov, R.K.; Mulyukov, R.R. Formation of Submicron Cone-Shaped Surface Morphology under Ion-Beam Sputtering of Nanostructured Nickel. *Tech. Phys. Lett.* **2022**, *48*, 55. [CrossRef]
9. Borisov, A.M.; Mashkova, E.S.; Ovchinnikov, M.A.; Khisamov, R.K.; Mulyukov, R.R. Ion-Induced Electron Emission and Surface Erosion of Nanostructured Nickel under High-Fluence Irradiation with 30-keV Argon Ions. *J. Surf. Investig.* **2021**, *15*, S66–S72. [CrossRef]

10. Andrianova, N.N.; Borisov, A.M.; Ovchinnikov, M.A.; Khisamov, R.K.; Mulyukov, R.R. Effect of Deformation Nanostructuring on the Ion-Beam Erosion of Copper. *J. Surf. Investig.* **2024**, *18*, 305–312. [CrossRef]
11. Khisamov, R.K.; Andrianova, N.N.; Borisov, A.M.; Ovchinnikov, M.A.; Mulyukov, R.R. Effect of Grain Size and Texture of Polycrystalline Tungsten on Its Ion-Beam Sputtering. *J. Surf. Investig.* **2025**, *19*, 179–189. [CrossRef]
12. Andrianova, N.N.; Borisov, A.M.; Ovchinnikov, M.A.; Khisamov, R.K.; Mulyukov, R.R. Effect of Deformation Nanostructuring on Ion-Beam Erosion of Metals. *Bull. Russ. Acad. Sci. Phys.* **2024**, *88*, 478–484. [CrossRef]
13. Rahman, M.; Chetri, S.; Teo, S.H.B.; Thompson, M.; Bilokur, M.; Corr, C.; Shekhar, S.; Temmerman, G.D.; Kakati, M. Studies on the retarded recrystallization of tungsten in CIMPLE-PSI exposed under very-high target temperature and long He^+-fluence. *Nucl. Fusion* **2025**, *65*, 16017. [CrossRef]
14. Borisov, A.M.; Mashkova, E.S.; Ovchinnikov, M.A.; Khisamov, R.K.; Musabirov, I.I.; Shayakhmetov, R.U.; Mulyukov, R.R. Increasing Thermal Stability of the Surface of Submicrocrystalline Nickel under High-Fluence Ion Irradiation. *J. Surf. Investig.* **2023**, *17*, 54–58. [CrossRef]
15. Zhang, X.D.; Hao, S.Z.; Grosdidier, T.; Zou, J.X.; Gao, B.; Bolle, B.; Allain-Bonasso, N.; Qin, Y.; Li, X.N.; Dong, C. Surface Modification of Light Alloys by Low-Energy High-Current Pulsed Electron Beam. *J. Metall.* **2012**, *2012*, 762125. [CrossRef]
16. Elbourne, A.; Coyle, V.E.; Truong, V.K.; Sabri, Y.M.; Kandjani, A.E.; Bhargava, S.K.; Ivanova, E.P.; Crawford, R.J. Multi-Directional Electrodeposited Gold Nanospikes for Antibacterial Surface Applications. *Nanoscale Adv.* **2019**, *1*, 203–212. [CrossRef] [PubMed]
17. Mulyukov, R.R.; Khisamov, R.K.; Baimova, J.A.; Borisov, A.M.; Baymiev, A.K.; Musabirov, I.I.; Ovchinnikov, M.A.; Safarov, I.M.; Timiryaev, R.R. Novel approach to obtain antibacterial nanospike surface by titanium bulk nanostructuring followed by ion irradiation. *Mater. Lett.* **2024**, *377*, 137455. [CrossRef]
18. Malis, O.; Brock, J.D.; Headrick, R.L.; Yi, M.S.; Pomeroy, J.M. Ion-induced pattern formation on Co surfaces: An x-ray scattering and kinetic Monte Carlo study. *Phys. Rev. B* **2002**, *66*, 35408. [CrossRef]
19. Girka, O.; Bizyukov, O.; Bogatyrenko, S.; Bizyukov, I. Aluminium Surface Morphology Behaviour under High-Flux Helium Ion Bombardment. *Nucl. Instrum. Methods Phys. Res. Sect. B Beam Interact. Mater. At.* **2017**, *405*, 31–35. [CrossRef]
20. Jiang, W.; Zhu, Y.; Zhang, L.; Edwards, D.J.; Overman, N.R.; Nandipati, G.; Setyawan, W.; Henager, C.H.; Kurtz, R.J. Dose Rate Effects on Damage Accumulation and Void Growth in Self-Ion Irradiated Tungsten. *J. Nucl. Mater.* **2021**, *550*, 152905. [CrossRef]
21. Girka, O.; Bizyukov, O.; Balkova, Y.; Myroshnyk, M.; Bizyukov, I.; Bogatyrenko, S. Ion Induced Millimetre-Scale Structures Growth on Metal Surfaces. *Nucl. Instrum. Methods Phys. Res. Sect. B Beam Interact. Mater. At.* **2018**, *420*, 46–49. [CrossRef]
22. Liu, Y.; McElroy, T.O.; Xia, C.; Wazeer, A.; Jacobson, M.; Xue, Y.; Lin, G.; Graening, T.; Yu, X.-Y.; Wang, H.; et al. Radiation Damage in Tungsten under High-Energy He-Ion Irradiation. *Commun. Mater.* **2026**, *7*, 140. [CrossRef]
23. Xue, M.; Yao, Y.; Ou, J.; Wang, F.; Qu, Y.; Li, W. Effect of Surface Roughness on Electron Work Function of AZ31 Mg Alloy and Their Correlation. *J. Alloys Compd.* **2018**, *731*, 44–48. [CrossRef]
24. Aghili, B.; Rahbarpour, S.; Berahman, M.; Horri, A. Influence of Surface Roughness on the Work Function of Gold: A Density Functional Theory Study. *J. Phys. Chem. C* **2024**, *128*, 8077–8084. [CrossRef]
25. Luo, Y.; Tang, Y.; Chung, T.-F.; Tai, C.-L.; Chen, C.-Y.; Yang, J.-R.; Li, D.Y. Electron Work Function: An Indicative Parameter towards a Novel Material Design Methodology. *Sci. Rep.* **2021**, *11*, 11565. [CrossRef] [PubMed]
26. Siebenhofer, M.; Nenning, A.; Rameshan, C.; Blaha, P.; Fleig, J.; Kubicek, M. Engineering Surface Dipoles on Mixed Conducting Oxides with Ultra-Thin Oxide Decoration Layers. *Nat. Commun.* **2024**, *15*, 1730. [CrossRef] [PubMed]
27. Kistanov, A.A. Atomic Insights into the Interaction of N_2, CO_2, NH_3, NO, and NO_2 Gas Molecules with Zn_2 (V, Nb, Ta)N_3 Ternary Nitride Monolayers. *Phys. Chem. Chem. Phys.* **2024**, *26*, 13719–13730. [CrossRef] [PubMed]
28. Yeh, C.-H.; Lin, Y.-J.; Reyes, Y.I.A.; Huang, Y.-H.; Coluccini, C.; Chen, H.-Y.T. Understanding Surface Reconstruction Mechanisms across Semiconductors, Metals, and Metal Oxides: A Review. *Appl. Surf. Sci. Adv.* **2026**, *34*, 101016. [CrossRef]
29. Lin, L.; Jacobs, R.; Ma, T.; Chen, D.; Booske, J.; Morgan, D. Work Function: Fundamentals, Measurement, Calculation, Engineering, and Applications. *Phys. Rev. Appl.* **2023**, *19*, 37001. [CrossRef]
30. Xue, M.; Wang, W.; Wang, F.; Ou, J.; Li, C.; Li, W. Understanding of the Correlation between Work Function and Surface Morphology of Metals and Alloys. *J. Alloys Compd.* **2013**, *577*, 1–5. [CrossRef]
31. Giannozzi, P.; Baroni, S.; Bonini, N.; Calandra, M.; Car, R.; Cavazzoni, C.; Ceresoli, D.; Chiarotti, G.L.; Cococcioni, M.; Dabo, I.; et al. QUANTUM ESPRESSO: A Modular and Open-Source Software Project for Quantum Simulations of Materials. *J. Phys. Condens. Matter* **2009**, *21*, 395502. [CrossRef] [PubMed]
32. Giannozzi, P.; Andreussi, O.; Brumme, T.; Bunau, O.; Buongiorno Nardelli, M.; Calandra, M.; Car, R.; Cavazzoni, C.; Ceresoli, D.; Cococcioni, M.; et al. Advanced Capabilities for Materials Modelling with Quantum ESPRESSO. *J. Phys. Condens. Matter* **2017**, *29*, 465901. [CrossRef] [PubMed]
33. Vanderbilt, D. Soft Self-Consistent Pseudopotentials in a Generalized Eigenvalue Formalism. *Phys. Rev. B* **1990**, *41*, 7892–7895. [CrossRef] [PubMed]
34. Garrity, K.F.; Bennett, J.W.; Rabe, K.M.; Vanderbilt, D. Pseudopotentials for High-Throughput DFT Calculations. *Comput. Mater. Sci.* **2014**, *81*, 446–452. [CrossRef]

35. Prandini, G.; Marrazzo, A.; Castelli, I.E.; Mounet, N.; Marzari, N. Precision and Efficiency in Solid-State Pseudopotential Calculations. *npj Comput. Mater.* **2018**, *4*, 72. [CrossRef]
36. Available online: https://next-gen.materialsproject.org/materials/mp-91?chemsys=W (accessed on 11 July 2026).
37. Davey, W.P. Precision Measurements of the Lattice Constants of Twelve Common Metals. *Phys. Rev.* **1925**, *25*, 753–761. [CrossRef]
38. Kishore, N.; Sudheer Kumar, B.; Manoj, K.N.V.K.; Balamurugan, D.; Sriram, S. Mechanical Properties of Tungsten-Rhenium, Lanthanum and Copper Doped Tungsten-Rhenium Nanostructures—A DFT Study. *Mater. Sci. Eng. B* **2022**, *278*, 115626. [CrossRef]
39. Hart, M.; Cernik, R.J.; Parrish, W.; Toraya, H. Lattice-Parameter Determination for Powders Using Synchrotron Radiation. *J. Appl. Crystallogr.* **1990**, *23*, 286–291. [CrossRef]
40. Kistanov, A.A.; Kosarev, I.V.; Shcherbinin, S.A.; Shapeev, A.V.; Korznikova, E.A.; Dmitriev, S.V. Unified Approach to Generating a Training Set for Machine Learning Interatomic Potentials: The Case of BCC Tungsten. *Mater. Today Commun.* **2025**, *42*, 111437. [CrossRef]
41. Van Riemsdijk, W.H.; Hiemstra, T. The CD-MUSIC Model as a Framework for Interpreting Ion Adsorption on Metal (Hydr) Oxide Surfaces. In *Interface Science and Technology*; Elsevier: Amsterdam, The Netherlands, 2006; Volume 11, pp. 251–268.
42. Gu, K.; Pang, M.; Zhan, Y. Insight into the Structural and Electronic Properties of Orthorhombic Cr 3 C 2 (001) Surface. *J. Phys. Chem. Solids* **2018**, *118*, 68–72. [CrossRef]
43. Tran, R.; Xu, Z.; Radhakrishnan, B.; Winston, D.; Sun, W.; Persson, K.A.; Ong, S.P. Surface Energies of Elemental Crystals. *Sci. Data* **2016**, *3*, 160080. [CrossRef] [PubMed]
44. Marcus, P.; Protopopoff, É.; Maurice, V. Surface Chemistry and Passivation of Metals and Alloys. In *Mechanics—Microstructure—Corrosion* Coupling; Elsevier: Amsterdam, The Netherlands, 2019; pp. 91–120.
45. Khoramian, R.; Issakhov, M.; Pourafshary, P.; Gabdullin, M.; Sharipova, A. Surface Modification of Nanoparticles for Enhanced Applicability of Nanofluids in Harsh Reservoir Conditions: A Comprehensive Review for Improved Oil Recovery. *Adv. Colloid Interface Sci.* **2024**, *333*, 103296. [CrossRef] [PubMed]
46. Fu, B.-Q.; Liu, W.; Li, Z.-L. Calculation of the Surface Energy of Bcc-Metals with the Empirical Electron Theory. *Appl. Surf. Sci.* **2009**, *255*, 8511–8519. [CrossRef]
47. Ran, G.; Liu, X.; Wu, J.; Zu, X.; Wang, L. The Effect of Surface Roughness on Self-Assembly Tungsten Nanoneedles Induced by Focused Ga+ Ion Beam Bombardment. *Appl. Surf. Sci.* **2012**, *258*, 5553–5557. [CrossRef]
48. Xue, M.; Peng, S.; Wang, F.; Ou, J.; Li, C.; Li, W. Linear Relation between Surface Roughness and Work Function of Light Alloys. *J. Alloys Compd.* **2017**, *692*, 903–907. [CrossRef]
49. Tran, R.; Li, X.-G.; Montoya, J.H.; Winston, D.; Persson, K.A.; Ong, S.P. Anisotropic Work Function of Elemental Crystals. *Surf. Sci.* **2019**, *687*, 48–55. [CrossRef]
50. Wang, Y.; Xu, L.; Hsu, H.-Y.; Leung, T.-C.; Lin, M.-C. First-Principles Study of Clean Tungsten Surface Work Function under Electric Field. *J. Vac. Sci. Technol. B Nanotechnol. Microelectron. Mater. Process. Meas. Phenom.* **2020**, *38*, 22209. [CrossRef]
51. Ma, Y.; Li, W.; Hu, J.; Zhang, X.; Xu, Y.; Lei, G.; Geng, S.; Liu, H.; Wang, X.; Huang, J.; et al. Investigating the Stability and Work Function Effects of Ba Atoms Adsorption on the Mo (110) Surface. *Nucl. Mater. Energy* **2025**, *45*, 101984. [CrossRef]
52. Huang, S.F.; Chang, R.S.; Leung, T.C.; Chan, C.T. Cohesive and Magnetic Properties of Ni, Co, and Fe on W(100), (110), and (111) Surfaces: A First-Principles Study. *Phys. Rev. B* **2005**, *72*, 75433. [CrossRef]
53. Zojer, E.; Taucher, T.C.; Hofmann, O.T. The Impact of Dipolar Layers on the Electronic Properties of Organic/Inorganic Hybrid Interfaces. *Adv. Mater. Inter* **2019**, *6*, 1900581. [CrossRef]
54. Kim, J.W.; Kim, A. Absolute Work Function Measurement by Using Photoelectron Spectroscopy. *Curr. Appl. Phys.* **2021**, *31*, 52–59. [CrossRef]
55. Luo, G.-N.; Yamaguchi, K.; Terai, T.; Yamawaki, M. Work Function Change of First Wall Candidate Metals Due to Ion Beam Irradiation. *J. Nucl. Mater.* **2001**, *290–293*, 116–120. [CrossRef]
56. Leite, F.L.; Bueno, C.C.; Da Róz, A.L.; Ziemath, E.C.; Oliveira, O.N. Theoretical Models for Surface Forces and Adhesion and Their Measurement Using Atomic Force Microscopy. *Int. J. Mol. Sci.* **2012**, *13*, 12773–12856. [CrossRef] [PubMed]
57. White, J.J.; Liu, J.; Hinsch, J.J.; Wang, Y. Theoretical Understanding of the Properties of Stepped Iron Surfaces with van Der Waals Interaction Corrections. *Phys. Chem. Chem. Phys.* **2021**, *23*, 2649–2657. [CrossRef] [PubMed]
58. De Andrade, A.M.; Kullgren, J.; Broqvist, P. Controlling the Metal Work Function through Atomic-Scale Surface Engineering. *Appl. Surf. Sci.* **2022**, *589*, 152932. [CrossRef]